


# Late-Holocene Indian summer monsoon variability revealed from a 3300-year-long lake sediment record from Nir'pa Co, southeastern Tibet

The Holocene  
1–12  
© The Author(s) 2016  
Reprints and permissions:  
sagepub.co.uk/journalsPermissions.nav  
DOI: 10.1177/0959683616670220  
hol.sagepub.com  


Broxton W Bird,<sup>1</sup> Yanbin Lei,<sup>2,3</sup> Melanie Perello,<sup>1</sup>  
Pratigya J Polissar,<sup>4</sup> Tandong Yao,<sup>2,3</sup> Bruce Finney,<sup>5</sup> Daniel Bain,<sup>6</sup>  
David Pompeani<sup>6</sup> and Lonnie G Thompson<sup>7</sup>

## Abstract

Sedimentological and geochemical results from Nir'pa Co, an alpine lake on the southeastern Tibetan Plateau, detail late-Holocene Indian summer monsoon (ISM) hydroclimate during the last 3300 years. Constrained by modern calibration, elevated silt and lithics and low sand and clay between 3.3 and 2.4 ka and 1.3 ka and the present indicate two pluvial phases with lake levels near their current overflow elevation. Between 2.4 and 1.3 ka, a sharp increase in sand and corresponding decrease in lithics and silt suggest drier conditions and lower lake levels at Nir'pa Co. Hydroclimate expressions in the sedimentological proxies during the Medieval Climate Anomaly (MCA) and 'Little Ice Age' (LIA) are not statistically significant, suggesting that these events were minor compared to the millennial scale variability on which they were superimposed. However, decreasing sand and increasing lithics and silt during the MCA between 950 and 800 cal. yr BP may suggest briefly wetter conditions, while increasing sand and reduced lithics and silt from 500 to 200 cal. yr BP suggest potentially drier conditions during the LIA. Similarities with regional records from lake sediment and ice cores and speleothem records from the central and eastern Tibetan Plateau, India, and the Arabian Sea, suggest generally coherent late-Holocene ISM variability in these regions. Increased late-Holocene ISM intensity occurred during times when Tibetan Plateau surface air temperatures were warmer, Indo-Pacific sea surface temperatures were elevated, and the tropical Pacific was in a La Niña-like mean state. Conversely, aridity between 2.4 and 1.3 ka occurred in concert with cooling on the Tibetan Plateau and in the Indo-Pacific with more El Niño-like conditions in the tropical Pacific. Differences with western Tibetan records may reflect a weakened ISM and stronger westerlies in this region during the late-Holocene.

## Keywords

drought, hydroclimate, 'Little Ice Age', Medieval Climate Anomaly, paleoclimate, pluvial, sedimentology, Third Pole Environment

Received 25 January 2016; revised manuscript accepted 22 July 2016

## Introduction

Holocene paleoclimate records from the Tibetan Plateau and surrounding regions, an area referred to as the Third Pole Environment (Qiu, 2008), show that the Indian summer monsoon (ISM) reached a maximum during the early- and middle-Holocene between 10 and approximately 6 ka when Boreal summer insolation peaked and strong tropical Pacific sea surface temperature (SST) gradients resembled a La Niña-like mean state (Bird et al., 2014; Cai et al., 2012; He et al., 2004; Koutavas et al., 2006; Marchitto et al., 2010; Morrill et al., 2003; Yanhong et al., 2006). The late-Holocene, in contrast, has been characterized by increasing aridity as summer insolation waned and an increasingly El Niño-like mean state developed in the tropical Pacific. Despite an improved understanding of long-term Holocene ISM trends and the likely driving mechanisms, higher frequency ISM variations have been more difficult to characterize because there are comparatively few high-resolution records from the Third Pole (Chen et al., 2015). The late-Holocene is underrepresented by high-resolution paleoclimate records in part because mean state aridity resulted in decreased resolution (e.g. Bird et al., 2014) or depositional hiatuses in many ISM archives (Berkelhammer et al., 2012;

Cai et al., 2012; Morrill et al., 2006). The paucity of climate records detailing ISM variability during the last few millennia limits our understanding of monsoon dynamics during a time

<sup>1</sup>Department of Earth Sciences, Indiana University–Purdue University Indianapolis, USA

<sup>2</sup>Key Laboratory of Tibetan Environment Changes and Land Surface Processes, Institute of Tibetan Plateau Research, Chinese Academy of Sciences, China

<sup>3</sup>CAS Center for Excellence in Tibetan Plateau Earth System, China

<sup>4</sup>Lamont-Doherty Earth Observatory, Columbia University, USA

<sup>5</sup>Department of Biological Sciences, Idaho State University, USA

<sup>6</sup>Department of Geology and Environmental Science, University of Pittsburgh, USA

<sup>7</sup>Byrd Polar Research Center, The Ohio State University, USA

## Corresponding author:

Broxton W Bird, Department of Earth Sciences, Indiana University–Purdue University Indianapolis, 723 W. Michigan SL 118, Indianapolis, IN 46202, USA.

Email: bwbird@iupui.edu

when climatic boundary conditions were generally similar to the present, but perturbations in radiative and other forcings, including ocean–atmosphere processes, produced widely recognized climatic events including the Medieval Climate Anomaly (MCA; AD 950–1250) and ‘Little Ice Age’ (LIA; AD 1450–1900; Mann et al., 2009).

Paleoclimate records from the Third Pole that span at least part of the late-Holocene suggest that within this period of general aridity, there were regional scale fluctuations in ISM precipitation, lake levels, and temperature (Bird et al., 2014; Herzsuh et al., 2006; Mischke and Zhang, 2010). Similar variability observed on longer timescales in Holocene-length paleoclimate records suggests that sub-orbital climate changes may be influenced by a variety of direct and indirect factors, including solar variability (Cai et al., 2012), Atlantic and Indo-Pacific ocean–atmosphere teleconnections (Bird et al., 2014; Chen et al., 2015; Goswami et al., 2006; Hong et al., 2003), and Tibetan Plateau surface air temperatures (Bird et al., 2014). At Paru Co, an alpine lake in the monsoon-dominated southeastern Tibetan Plateau, Bird et al. (2014) noted that low lake stands and high hydrogen isotopic compositions of sedimentary leaf waxes ( $\delta D_{wax}$ ) coincided with warmer Indo-Pacific SST (Koutavas et al., 2006; Stott et al., 2004), cooler eastern equatorial Pacific SST (Marchitto et al., 2010) and elevated surface air temperatures on the central Tibetan Plateau (Herzsuh et al., 2006). The opposite associations were noted during low lake stands. Late-Holocene aridity on the Third Pole occurred within the context of more El Niño-like Pacific SST structure and cooling over the Tibetan Plateau (Bird et al., 2014). Centennial lake-level variability followed this general warm-wet, cool-dry pattern. Persistently, low lake levels at Paru Co during the late-Holocene, however, limited the lake’s sensitivity to hydroclimate changes, making it difficult to discern ISM variability at centennial or shorter timescales. Because many other records also lose resolution during this time, the role that regional SAT and/or Indo-Pacific SST played in ISM variability during the last ~4000 years is not well defined. Filling this gap in knowledge is important because changes in radiative forcing and ocean–atmosphere systems, particularly during the MCA and LIA, have been suggested to have produced significant precipitation anomalies in the East Asian and South American monsoon systems (Bird et al., 2011; Chen et al., 2015; Zhang et al., 2008). In the ISM region, however, hydroclimatic signatures of the MCA and LIA in paleoclimate records are more equivocal. Some records, such as accumulation at Dasoupu (Thompson et al., 2000) and  $\delta^{18}O$  from Dandak Cave (India; Sinha et al., 2006) and Sahiya Cave (Sinha et al., 2015), suggest possibly wetter conditions during the MCA and drier conditions during the LIA, while other studies suggest the opposite (Liu et al., 2009). Excluding the Third Pole, the MCA and LIA appear to have produced an east–west hydroclimate dipole response north of 30°N whereby northwest and central Asia were drier and northern to northeastern China wetter during the MCA (Chen et al., 2015). The opposite conditions are suggested for the LIA. In order to help resolve questions regarding late-Holocene ISM dynamics and their relationships with hydroclimate variability across Asia, additional records from core ISM regions are needed.

To this end, we present a 3300-year-long multi-proxy hydroclimate record from Nir’pa Co that details the hydroclimatic variability of a region highly sensitive to changes in ISM precipitation. Through comparison with existing paleoclimate records from the Third Pole and other climatically significant regions, we investigate the regional expression of late-Holocene ISM precipitation (including the MCA and LIA), its relationship with known climatic and ocean–atmosphere influences, and whether Indo-Pacific and El Niño–Southern Oscillation (ENSO)-like forcing mechanisms of ISM variability suggested for the early- and middle-Holocene can similarly account for late-Holocene ISM variations.

### Study area: Nir’pa Co

Nir’pa Co is a small (0.1 km<sup>2</sup>) alpine lake situated at 4775 m a.s.l. in the Nyainqêntanglha Mountains on the southeastern Tibetan Plateau (Figures 1 and 2a; 29.734°N, 92.386°E). Nir’pa Co’s watershed is defined by a 5.38-km-long and 1.3-km-wide glacially carved valley that trends northwest–southeast with a maximum elevation of 5150 m a.s.l. (Figure 2a). This valley is part of a larger plateau that contains numerous glacial features, such as moraines and glacial lakes, including Paru Co (Bird et al., 2014). The local bedrock is geologically homogeneous, consisting of Pleistocene age andesite (Choubert et al., 1983). The lake is deep relative to others in the area, with a maximum depth of 18.6 m. Nir’pa Co’s bathymetry is generally steep sided with a flat bottom that is deepest near the center of the lake (Figure 2b). An ephemeral stream enters on the lake’s northwestern shore, at which point it forms a delta on a shallow littoral shelf (Figure 2b). A channel at the lake’s southeast shore provides an outlet for overflow that has incised into the terminal glacial moraine that dams the lake. This outlet was overflowing, albeit with restricted flow, when cores were collected from Nir’pa Co in May 2011 and June 2015, suggesting that the lake is currently at or near its maximum surface elevation but becomes seasonally restricted.

ISM moisture largely derived from the Bay of Bengal is the primary source of precipitation for regions of the Tibetan Plateau between the Himalayan and Tanggula Mountains and for interior monsoonal regions in India (Sinha et al., 2015; Tian et al., 2001, 2007). Consistent with this, 92% of mean annual precipitation at Nir’pa Co occurs during the monsoon season with peaks between May and September when temperatures rise above freezing and the lake is ice free and sediment can be transported from the watershed and deposited in Nir’pa Co (Figure 2c; Bird et al., 2014; Lawrimore et al., 2011; Peterson and Vose, 1997). Precipitation during the remainder of the year accounts for only 8% of the annual hydrologic budget and is received primarily as snow when average monthly temperatures are near or below 0°C from November through April. During these months, Nir’pa Co is covered with ice, limiting sediment input to the lake. Tropical Rainfall Measuring Mission (TRMM – 3B43) precipitation data estimates suggest regional annual rainfall totals 1118 mm yr<sup>-1</sup>, while instrumental weather station data indicate annual rainfall amounts to 479 mm yr<sup>-1</sup>. The difference between these amounts may be due in part to overestimations of rainfall at elevation by TRMM data and underestimations of rainfall at elevation based on rainfall gauge measurements made in valleys. Regardless, the majority of precipitation at Nir’pa Co in either data set occurs during the summer monsoon season when the lake is ice free and sediment can be mobilized from the lake’s catchment and transported to Nir’pa Co via fluvial processes.

A number of ocean–atmosphere and terrestrial climate feedbacks influence ISM precipitation (Ashok et al., 2004; Peings and Douville, 2010; Shaman and Tziperman, 2005). Interannual Indo-Pacific ocean–atmosphere variability associated with the ENSO is a primary modulator of ISM rainfall (Ashok et al., 2004; Gadgil, 2003; Krishnamurthy and Kirtman, 2009; Kumar et al., 2006). Observational records show that cooling in the Indo-Pacific during El Niño events coincides with increased atmospheric subsidence and reduced precipitation over the Asian monsoon region. During La Niña events, warm Indo-Pacific SST enhances convergence and vertical air motion over the Asian monsoon region, thereby contributing to enhanced monsoon rainfall. ENSO-like mechanisms have been invoked on longer timescales to explain multi-decadal to millennial trends in ISM and Asian monsoon rainfall, whereby persistent El Niño or La Niña-like conditions in the tropical Pacific created background conditions of either persistently stronger or weaker monsoon circulation over Asia (Bird et al., 2014; Hong et al., 2005; Krishnan and Sugi, 2003).

The Indian Ocean Dipole (IOD) is another recognized driver of ISM variability, which may also contribute to long-term trends

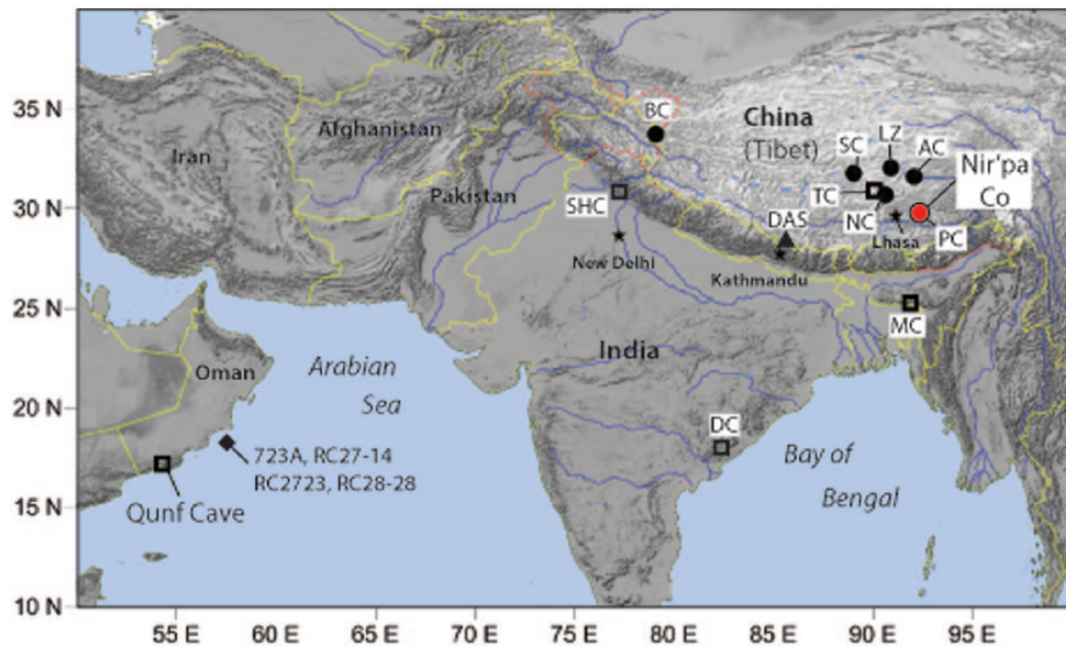


**Figure 1.** Map of the broader study region showing the location of paleoclimate sites discussed in the text. Nir'pa Co is marked with a red circle. Other lakes' records are indicated with black circles. Cave records are with a diamond. Abbreviations for paleoclimate records are as follows: PC: Paru Co; AC: Ahung Co; LZ: Lake Zigetang; SC: Seling Co; TC: Tianmen Cave; NC: Nam Co; MC: Mawmluh Cave; DC: Dandak Cave; DAS: Dasoupu; BC: Bangong Co; SHC: Sahiya Cave.

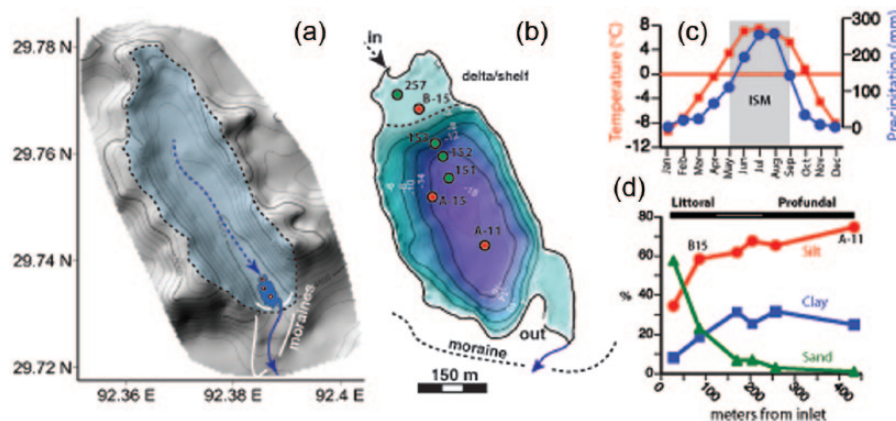


**Figure 2.** (a) Detailed digital elevation map of the Nir'pa Co watershed (outlined with a dashed line and shaded blue) showing the position of moraines (while solid lines), and seasonal (dashed blue line) and permanent streams (solid blue line). (b) Expanded view of Nir'pa Co showing the location of inflow (white dashed line) and outflow (solid white line), the delta/shelf at the lakes' north end, and the location from which cores A-11, A-15, and B-15 were collected (white circles). The location of surface samples from the transect is shown with green circles. (c) Monthly average temperature (red) and precipitation (blue) at Nir'pa Co (Bird et al., 2014). (d) Grain size results from surface sample transect sites (green circles in 2b).

in monsoon rainfall (Ashok et al., 2004). The IOD, however, is not wholly independent from ENSO and is considered by some to be an extension of ENSO variability in the Indian Ocean, albeit with some independent behavior (Ashok et al., 2001, 2004). Warm IOD events are typically associated with La Niñas and enhanced ISM rainfall. Cool IOD events are conversely associated with El Niño events and reduced ISM rainfall. The IOD's influence on ISM rainfall during the Holocene is not well known, however, because there are a limited number of SST reconstructions from key centers of IOD action in the Indian Ocean and none that continuously span the late-Holocene.

## Methods

### Sediment core and sample collection

A 90-cm surface core (A-11) was collected from Nir'pa Co in May 2011 in 17.5 m of water using an Aquatic Research

hammer core (Figure 2b). Two additional surface cores (A-15 and B-15) were acquired in June 2015 using a piston coring system in water depths of 16.5 and 1.0 m, respectively (Figure 2b). The top 10 cm of A-11 was extruded at 0.5 cm intervals in the field immediately following collection. Cores A-15 and B-15 were not extruded in the field, but instead secured with absorbent foam, which stabilized the sediments for transport. Visible stratigraphy in the upper portion of B-15 and the lack of void space in A-15 indicated that the sediments did not mix during transport. In order to characterize modern sediment distributions, grab samples of the upper 2 cm were collected using an Ekman grab sampler along a southeast–northwest transect that extended from the lake's profundal zone (18 m) to the inlet (0.6 m; Figure 2b). All cores and grab samples were stored at 4°C until they were analyzed at the Indiana University–Purdue University Indianapolis (IUPUI) Paleoclimatology and Sedimentology Laboratory.

### Initial core description

Surface cores were split, described, imaged, and volumetrically subsampled ( $1 \text{ cm}^{-3}$ ) at 2 cm intervals for %water, dry bulk density, and loss on ignition (LOI). Magnetic susceptibility (MS) was measured on the archive half of the cores using a Bartington MS2 MS meter with units  $\text{SI} \times 10^{-5}$ . Wet  $1 \text{ cm}^3$  samples were weighed, dried for 24 h at  $60^\circ\text{C}$ , and reweighed to determine dry bulk density ( $\rho_{\text{dry}}; \text{gcm}^{-3}$ ) and %water. Percent total organic matter (%TOM) and percent total carbonate (%TC) were determined by weight loss after combustion at  $550^\circ\text{C}$  (4 h) and  $1000^\circ\text{C}$  (2 h), respectively (modified from Heiri et al., 2001).

### Grain size

Approximately 1.0 g of wet sediment was collected from homogenized grab samples and at 1 cm intervals from surface cores A-11, dried for 24 h at  $60^\circ\text{C}$ , and weighed. Organic matter was removed prior to grain size analysis by soaking samples in a 50-mL aliquot of 35%  $\text{H}_2\text{O}_2$  at room temperature for 24 h before being treated sequentially with five 20 mL aliquots of 35%  $\text{H}_2\text{O}_2$  at  $65^\circ\text{C}$  (Gray et al., 2010). Biogenic silica was removed with a 20-mL 1-N NaOH digestion (6 hr at  $60^\circ\text{C}$ ) and verified by smear slide for 10% of the samples. Acid washing was not performed because LOI indicated that carbonate was not present. After freeze drying, the samples were soaked for 24 h in a 2.5% sodium metaphosphate solution. Particle size distributions of the lithic fraction were measured using a Malvern Mastersizer 2000 with reported values calculated using the average of three replicate measurements.

### Elemental and isotopic or organic carbon and sedimentary nitrogen

Homogenized subsamples at  $\sim 2$  cm intervals ( $n = 41$ ) from core A-11 were analyzed for total organic carbon (TOC), total nitrogen (TN) concentrations, and  $\delta^{13}\text{C}$  and  $\delta^{15}\text{N}$  using a Costech ECS 4010 elemental analyzer interfaced to a Thermo Delta V Advantage continuous flow isotope ratio mass spectrometer. Isotope ratios are reported in per mil units (‰) according to the relationship  $\delta X = [(R_{\text{sample}}/R_{\text{standard}}) - 1] \cdot 1000$ , where X is the element of interest and R is a measured isotopic ratio of either a sample or a standard. Carbon isotope measurements are relative to the Vienna Peedee Belemnite (VPDB) standard, and all nitrogen measurements are relative to atmospheric nitrogen. Replicate measurements of internal standards run during sample analysis yielded coefficients of variation of 4.4% and 6.9% for TOC and TN, respectively, and precision better than 0.2 ‰ for the isotopic data. Isotope measurements were made at Idaho State University.

### Biogenic silica and %lithics

Biogenic silica was quantitatively determined on samples at  $\sim 2$  cm resolution ( $n = 41$ ) from A-11 using a wet-alkali dissolution method (0.1 M  $\text{Na}_2\text{CO}_3$  at  $85^\circ\text{C}$  for 5 h) modified from Mortlock and Froelich (1989) and measured by molybdate-blue spectrophotometry. Values are reported as 10% hydrated silica ( $\text{SiO}_2 \cdot 0.4 \text{ H}_2\text{O}$ ) using a multiplier of 2.4 times the weight percent of biogenic silica content (Mortlock and Froelich, 1989). An estimated error of  $<4.6\%$  (calculated as the coefficient of variation) is based on replicate measurements of two internal sediment standards.

The lithic abundance was calculated by subtracting percent abundances of biogenic silica and %TOM from 100% assuming that carbonate was not a significant sediment constituent based on LOI data.

### Scanning x-ray fluorescence geochemistry

Sedimentary titanium (Ti) concentrations were determined by scanning x-ray fluorescence (XRF) using an ITRAX XRF

scanner at the University of Minnesota, Duluth (see supplemental information for concentrations of other elements measured, available online). Measurements were made at 0.5 cm increments with a molybdenum x-ray tube and a sample exposure time of 15 s per spot. Values are reported as counts per second (cps) where greater elemental concentrations correspond to higher cps.

### Geochemistry

Two samples composed of bedrock and glacial till from the adjacent Paru Co watershed and one of bedrocks from the Nir'pa Co watershed were analyzed by ALS Global for a suite of elements, of which only Ti is discussed here (see supplemental materials for other elements measured and concentrations, available online). Following ultra-trace level method ME-MS61, approximately 0.25 g of sample was digested using perchloric, nitric, and hydrofluoric acids with the residue leached with dilute hydrochloric acid and diluted to volume. Measurements were made by inductively coupled plasma-atomic emission spectrometry and inductively coupled plasma-mass spectrometry with results corrected for spectral inter-element interferences (Table S1, available online).

### Powder x-ray diffraction

The mineralogical composition of four samples, three from core A-11 at 7, 45, and 93 cm and one of bedrocks from Nir'pa Co's watershed, was analyzed using powder x-ray diffraction (XRD). The XRD analyses were conducted using a Bruker D8 Discover instrument, equipped with an IAS Cu microsource of 1.54 Å wavelength which provided an x-ray beam through a 2-mm point collimator. The XRD pattern was detected by a LynxEye one-dimensional (1D) detector. The x-ray source's operating conditions were voltage of 50 kV and current of 1000  $\mu\text{A}$ . Qualitative mineral phase identification was performed using Bruker's Diffrac.EVA software and the Crystallographic Open Database (COD; Table S2, available online).

### Sediment age

Surface sediments from core A-11 were dated using  $^{210}\text{Pb}$ ,  $^{214}\text{Pb}$ , and  $^{137}\text{Cs}$  measured by direct gamma counting on 10 samples from the upper 9.5 cm (Table 1; Appleby and Oldfield, 1983; Schelske et al., 1994). Radiocarbon ages from A-11 ( $n = 2$ ) and B-15 ( $n = 2$ ) were determined by accelerator mass spectrometry (AMS;  $^{14}\text{C}$ ) at the University of California, Irvine (UCI), Keck AMS Facility on samples consisting of charcoalized grass fragments, which were isolated by wet sieving sediment at  $63 \mu\text{m}$  (Table 2). The samples were manually cleaned and chemically pretreated with an acid-alkali-acid wash of 1 N HCl and 1 N NaOH following UCI protocols. Radiocarbon ages were calibrated with the online program CALIB 6.0 (Stuiver and Reimer, 1993) using the IntCal 09.14c data set. We report the median probability age and  $2\sigma$  error as thousands of calendar years (ka) before present (BP; present = AD 1950).

## Results

### Lithology

Surface core A-11 is characterized by reddish-brown, fine-grained sediment that becomes progressively darker reddish brown with depth. Banding was noted in the upper 30 cm and below 60 cm. Scattered organic fragments, including grass and charcoal, are visible throughout the core. Sediments in surface core A-15 were dark to medium gray with no apparent banding. In surface core B-15, sediments were gray and coarse grained with some banding distinguished by zones of increased organic matter from 94 to 74 cm.

**Table 1.**  $^{210}\text{Pb}$  and  $^{137}\text{Cs}$  results from Badi Namco core A-11.

| Mean depth (cm) | $^{210}\text{Pb}$ activity | $\pm$   | Supported $^{210}\text{Pb}$ or $^{214}\text{Pb}$ activity (Bq/g) | $\pm$ | Excess $^{210}\text{Pb}$ (Bq/g) | $\pm$ | $^{137}\text{Cs}$ activity (Bq/g) | $\pm$  | cal. yr BP |
|-----------------|----------------------------|---------|--|-------|---------------------------------|-------|-----------------------------------|--------|------------|
| 0.25            | 0.64                       | 0.077   | 0.113  | 0.014 | 0.527                           | 0.063 | <DET                              | 0      | -56        |
| 1.25            | 0.69                       | 0.077   | 0.093  | 0.011 | 0.597                           | 0.066 | <DET                              | 0      | -48        |
| 2.25            | 0.664                      | 0.0775  | 0.086  | 0.012 | 0.579                           | 0.065 | <DET                              | 0      | -38        |
| 3.25            | 0.616                      | 0.0735  | 0.112  | 0.016 | 0.504                           | 0.057 | <DET                              | 0      | -22        |
| 4.25            | 0.4                        | 0.0545  | 0.097  | 0.013 | 0.303                           | 0.042 | 0.0449                            | 0.0174 | -6         |
| 5.25            | 0.277                      | 0.0431  | 0.110  | 0.013 | 0.167                           | 0.030 | <DET                              | 0      | 12         |
| 6.25            | 0.229                      | 0.0417  | 0.119  | 0.013 | 0.110                           | 0.029 | <DET                              | 0      | 43         |
| 7.25            | 0.12                       | 0.02335 | 0.091  | 0.009 | 0.029                           | 0.015 | <DET                              | 0      | 64         |
| 8.25            | 0.128                      | 0.028   | 0.094  | 0.010 | 0.034                           | 0.018 | <DET                              | 0      | n/a        |
| 9.25            | 0.151                      | 0.03395 | 0.142  | 0.014 | 0.000                           | 0.020 | <DET                              | 0      | n/a        |

**Table 2.** Radiocarbon results from Nir'pa Co cores A-11 and B-15.

| UCI AMS # | Core | Depth (cm) | Fraction Modern | $\pm$  | $\Delta 14\text{C}$ (‰) | $\pm$ | 14C yr B.P. | $\pm$ | Cal yr B.P. | +/-   |
|-----------|------|------------|-----------------|--------|-------------------------|-------|-------------|-------|-------------|-------|
| 104262    | A-11 | 46–47      | 0.8551          | 0.0029 | -144.9                  | 2.9   | 1255        | 30    | 1210        | 70/40 |
| 104263    | A-11 | 88.5–89.5  | 0.6812          | 0.0030 | -318.8                  | 3.0   | 3085        | 40    | 3290        | 92/83 |
| 165845    | B-15 | 66–67      | 0.5809          | 0.0026 | -419.1                  | 2.6   | 4365        | 40    | 4930        | 60/80 |
| 165846    | B-15 | 90–91      | 0.2931          | 0.0014 | -706.9                  | 1.4   | 9860        | 40    | 11250       | 90/50 |

Macroscopic charcoal and organic matter were particularly visible from 94 to 81 cm. From 74 to 65 cm, B-15 sediments transition to a tan color with a darker brown band of mottled sediment between 69 and 65 cm. From 65 to 44 cm, sediments are tan and fine grained with some banding and still visible, but fewer organic particles. At 44 cm, macroscopic organic matter particles increased until 5 cm. Above 5 cm, the sediments are more olive green and the abundance of macroscopic plant fragments decreases.

### Chronology

Excess  $^{210}\text{Pb}$  ( $^{210}\text{Pb}_{\text{ex}}$ ) activities were highest in core A-11 between 0 and 3.5 cm. Below this depth,  $^{210}\text{Pb}_{\text{ex}}$  decays until reaching background activities at 7.5 cm. Using the constant rate of supply (CRS) model (Appleby and Oldfield, 1983), an age model was constructed for the upper most sediment depths between 0 and 7.5 cm (Figure 3). One sample at  $4.25 \pm 0.25$  cm contained measurable  $^{137}\text{Cs}$  activities. Based on the  $^{210}\text{Pb}$  CRS age model, this sample dates to 1950–1960  $\pm 4$  CE. Samples above and below this, which are dated at 1969–1977 CE and 1929–1940 CE, respectively, contain no measurable  $^{137}\text{Cs}$ . Although slightly pre-dating the 1963 CE  $^{137}\text{Cs}$  maximum, the 4.25 cm sample's age is within error of 1963 CE and consistent with the period during which atmospheric tests of nuclear weapons were being conducted, supporting the  $^{210}\text{Pb}$  CRS age model. Below 7.5 cm, two AMS  $^{14}\text{C}$  ages of charcoaled grass fragments anchor the core chronology. A second-order polynomial was fit to the combined  $^{210}\text{Pb}$  and AMS  $^{14}\text{C}$  ages to quantitatively establish the age–depth relationship, which spans the last 3.4 ka.

The polynomial age model's uncertainty was evaluated by comparing with an age model derived using the Bchron age modeling software (Blaauw and Christen, 2011; Figure S1, available online). The polynomial age model is well within the two-sigma confidence interval of the Bchron age model while a regression between the two age models yielded a slope of 1.01 and an  $r^2$  of 0.998. The Bchron age model, however, produces abrupt changes in sedimentation rates at the  $^{14}\text{C}$  age control points that are unlikely to reflect actual sedimentation rate changes. For this reason, we utilize the polynomial age model, which estimates more gradual changes in sedimentation rates.

The basal AMS  $^{14}\text{C}$  sample for core B-15 at 90 cm returned an age of 11.25 ka with the 66-cm sample returning an age of 4.5 ka (Table 1).

### Bulk density, LOI, and the elemental and isotopic composition of organic matter carbon and nitrogen

Dry bulk density for core A-11 averaged  $0.28 \text{ g cm}^{-3}$  during the last 3.3 ka with near average densities from 3.3 to 1.2 ka, above average densities between 1.2 ka and 60 cal. yr BP, and then a marked decrease to the present (Figure 4a). Mass accumulation rates averaged  $8.7 \times 10^{-3} \text{ g cm}^{-2} \text{ yr}^{-1}$  with a maximum of  $15.9 \times 10^{-3} \text{ g cm}^{-2} \text{ yr}^{-1}$  and a minimum of  $4.6 \times 10^{-3} \text{ g cm}^{-2} \text{ yr}^{-1}$  and shows a similar trend with slowly increasing rates from 3.3 to 1.2 ka, a steeper increase between 1.2 ka and 60 cal. yr BP, and a sharp drop-off to the present (Figure 4b).

Organic matter abundances averaged 13.3% and are characterized by a decreasing trend from 3.3 ka to 360 cal. yr BP that is marked by variations of up to  $\pm 4\%$ . After 360 cal. yr BP, percent organic matter (%OM) increased sharply to the present (Figure 4c). When considered as flux, organic matter deposition averaged  $1.1 \times 10^{-3} \text{ g cm}^{-2} \text{ yr}^{-1}$  with a maximum of  $1.9 \times 10^{-3} \text{ g cm}^{-2} \text{ yr}^{-1}$  and a minimum of  $0.6 \times 10^{-3} \text{ g cm}^{-2} \text{ yr}^{-1}$  and an increasing trend that is similar to that of mass accumulation (Figure 4d). Average carbonate content was less than 3%; variations in %TC most likely represent the loss of interstitial water from clays.

The atomic ratio of carbon to nitrogen (C:N) averaged 11.1 during the last 3.3 ka with a steady decreasing trend to the present although with variability ranging between 14.5 and 9.4 (Figure 4e). Biogenic silica concentrations averaged 10.8% with values ranging between 15.0% and 6.7% (Figure 4f). A slight decreasing trend is apparent over the length of the record, but with considerable variability. When plotted as flux, a generally increasing trend similar to organic matter flux is observed (Figure 4). Organic matter  $\delta^{13}\text{C}$  ( $\delta^{13}\text{C}_{\text{org}}$ ) was relatively constant during the last 3.3 ka, varying by less than 1‰ about a mean of  $-24.6\%$  until 80 cal. yr BP when  $\delta^{13}\text{C}_{\text{org}}$  decreased to  $-25.9\%$  (Figure 4g). The isotopic composition of sedimentary nitrogen averaged 2.6‰ and ranges from 3.1‰ to 2.1‰ (Figure 4h). The data suggest a generally increasing trend toward present, with highest values after 500 cal. yr BP

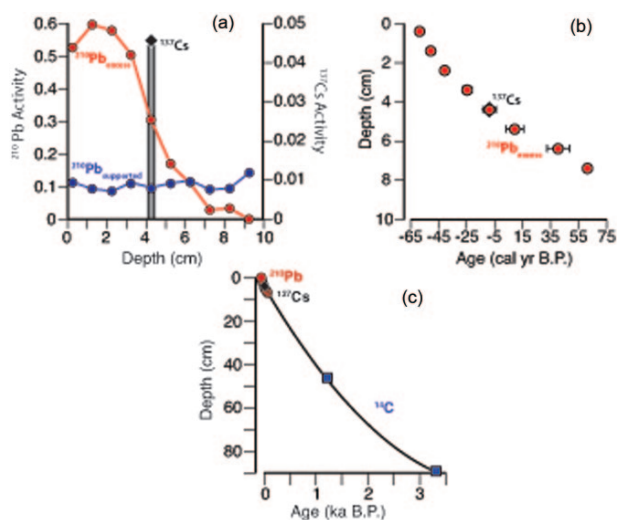


**Figure 3.** (a) Excess (red) and supported (blue)  $^{210}\text{Pb}$  activities versus depth with  $^{137}\text{Cs}$  activities are shown for the top 10 cm of core A-11. Where error bars are not visible, they are smaller than the symbol size. (b) Sediment depth ages based on the CRS age model are shown with the depth at which maximum  $^{137}\text{Cs}$  activity occurred (4.5 cm). (c) The composite age model for Nir'pa Co core A-11 with a second-order polynomial fit to the  $^{210}\text{Pb}$  (red circles) and AMS  $^{14}\text{C}$  (blue squares) ages with the  $^{137}\text{Cs}$  peak depth shown with a black diamond.

#### Lithics and grain size

Downcore lithic abundances in the Nir'pa Co record varied between 70.5% and 81.0% with an average of 75.0% (Figure 5a). Correlations were positive with Ti ( $r = 0.70$ ;  $p < 0.001$ ) and dry bulk density ( $r = 0.38$ ;  $p = 0.096$ ), null with %BSi, and negative with %TOM ( $r = -0.71$ ;  $p < 0.001$ ) as expected since %lithics was calculated from %TOM. Still the lithics–TOM correlation is not 1:1, suggesting there is some signal captured. The relationship between lithics and dry bulk density improves greatly ( $r = 0.64$ ;  $p < 0.001$ ) if the most recent 110 years are excluded from the regression, which may reflect the approximate time for flocculent sediment compaction to occur. Between 3.3 and 2.4 ka, %lithics was near average at 74.1% with low values between 3.3 and 2.9 ka and a peak between 2.9 and 2.4 ka. At 2.4 ka, %lithics decreased to an average of 73.8% until 1.3 ka, but with variability. After 1.3 ka, %lithics increased to 77.3%, but again with variability. Peaks in %lithics occurred at 0.9, 0.4, and 0.1 ka with intervening drops. The flux of lithic materials shows variations similar to %lithics, but with less variability prior to 1.3 ka. From 3.3 to 1.3 ka, values generally increased, ranging between 2.2 and  $10.1 \times 10^{-3} \text{ g cm}^{-2} \text{ yr}^{-1}$  about a mean of  $5.7 \times 10^{-3} \text{ g cm}^{-2} \text{ yr}^{-1}$ . After 1.3 ka, lithic flux increased more steeply plateauing at an average of  $8.4 \times 10^{-3} \text{ g cm}^{-2} \text{ yr}^{-1}$  by 950 cal. yr BP (Figure 5a). At 110 cal. yr BP, lithic flux began to decrease steeply to the present value of  $6.1 \times 10^{-3} \text{ g cm}^{-2} \text{ yr}^{-1}$ .

The grain size distribution of the lithic fraction is dominated by silt, which varies between 63.3% and 81.1% and averages 71.5% (Figure 5b). Between 3.3 and 2.4 ka, %silt was 2.4% below the mean, averaging 69%, before decreasing by a further 1–68% between 2.4 and 1.4 ka (Figure 5b and d). At 1.4 ka, %silt began a sustain increase to the present, increasing by 6–73.8%. Clay is the next most abundant grain size fraction, accounting for 27.6% of the lithic component on average with a range between 18.6% and 36.5% (Figure 5e). Clay and silt are strongly anti-correlated at a near 1:1 relationship ( $m = -1.01$ ;  $r^2 = 0.88$ ) over the duration of the record. Sand is the least abundant lithic constituent, averaging just 1.5%, but ranging between 0.0% and 5.6% (Figure 5c). Variations in %sand are distinct from those of

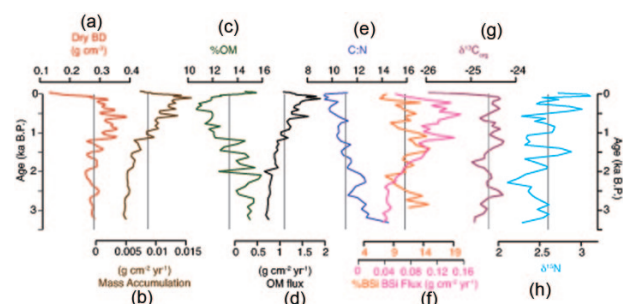


**Figure 4.** Sedimentological and geochemical results from Nir'pa Co core A-11: (a) dry bulk density, (b) mass accumulation, (c) percent organic matter, (d) organic matter flux, (e) the ratio of elemental carbon to nitrogen, (f) percent biogenic silica (orange) and flux (pink), (g)  $\delta^{13}\text{C}$  of organic matter, and (h)  $\delta^{15}\text{N}$  of sedimentary nitrogen. Vertical lines represent the late-Holocene mean of each record.

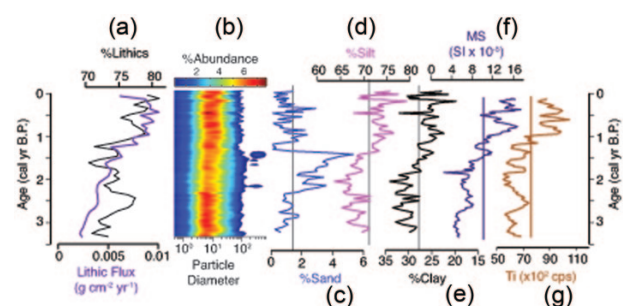


**Figure 5.** Physical sedimentology and XRF results from Nir'pa Co core A-11: (a) percent lithics and lithic flux, (b) histogram showing the downcore abundance distribution of clastic grain sizes, (c) percent sand, (d) percent silt, (e) percent clay on a reversed axis to highlight similarities with %silt, (f) magnetic susceptibility, and (g) XRF-derived Ti. Vertical lines as in Figure 4.

silt and clay, but with transitions between higher and lower concentrations coinciding with transitions in silt and clay. Between 3.3 and 2.4 ka and again between 1.4 ka and the present, %sand was generally low, averaging 1.1% and 1.0%, respectively. From 2.4 to 1.4 ka, %sand increased sharply, averaging 3% and reaching a maximum of 5.6%.

Surface grab samples show consistent relationships between grain size, depth, and distance along the sampling transect (Figure 2). As expected, %sand is highest in littoral region closest to the ephemeral inlet with peak values of 58%. Sand abundance decreased away from the inlet toward the middle of the lake with sand in profundal sites decreasing from 7% to less than 1% at the A-11 core site. Silt and clay abundances are lowest in the littoral zone and increase toward the center of the lake. Within the profundal zone, %silt and %clay are largely consistent across the transect, but with a subtle antiphased relationship.

#### Analytical and XRF Ti abundances

Geochemical analysis of the Nir'pa Co and Paru Co bedrock samples returned high Ti values of 2360 and 2460 ppm, respectively. Ti concentrations in the glacial till were similarly high, measuring 2290 ppm. Consistent with the sediment source geochemistry (i.e. bedrock), XRF-derived Ti in the Nir'pa Co sediment core was high, averaging 7190 cps between a range of 10,510 and 5460 cps (Figure 5g). Values of Ti were below average, but with variability, between 3.3 and 1.2 ka, after which time they increased to the top of the core. Both the long term and higher frequency Ti variability closely resemble %lithics variations ( $r = 0.70$ ;  $p < 0.001$ ).

### XRD mineralogy

XRD patterns from the bedrock sample indicate the presence of quartz, feldspars, muscovite, and titanite, consistent with its mapped andesitic composition. Accordingly, the downcore sediment samples from Nir'pa Co A-11 reflect this bedrock mineralogy, showing similar assemblages (mainly quartz, feldspar, muscovite, and titanite) with the addition of clay weathering products (Table S1, available online).

### MS

MSs for core A-11 averaged 10.1 during the record with a maximum of 17.5 and a minimum of 2.5 (Figure 5f). Values were generally low between 3.3 and 1.5 ka with the exception of a broad peak between 2.8 and 2.4 ka. After 1.5 ka, MS increased, but with superimposed centennial-scale variability that resembles that of the Si/Ti ratio noted above. For A-15, MS averaged 11.0 with a maximum of 16.1 and a minimum of 6.0. Trends similar to A-11 are noted in the A-15 MS with generally increasing values with decreasing depth and peaks from 70 to 75, 45 to 51, 31 and 38, and 10 to 21 cm (supplemental material, available online). Although the magnitude of the peaks in MS vary somewhat between the two cores, the correspondence is generally good considering that A-11 was collected from near the middle of the lake and A-15 was collected closer to the shore where the profundal zone begins to slope up toward the shore.

## Discussion

We focus on results from A-11 because its profundal location is less likely to be affected by internal lake processes, such as near-shore currents, which could affect sediment characteristics (i.e. the location of A-15). Similarities between A-11 and A-15, however, support generally consistent sedimentation across the lake basin, which give us confidence that the A-11 results are representative of the lake's hydroclimate variations during the late-Holocene (Figure S3, available online). Core B-15 is not included in the discussion because the initial  $^{14}\text{C}$  results indicate that it likely contains hiatuses and is not a complete record of Holocene climate. Nonetheless, the basal age of 11.25 ka is consistent with the basal age from nearby Paru Co, suggesting that lakes in the region deglaciated and filled rapidly at this time.

### Lithic and grain size proxy interpretation

Grain size measurements of lacustrine sediments offer insight into watershed and in-lake processes that are sensitive to climatic variations (e.g. Conroy et al., 2008; Dearing, 1997; Shuman et al., 2009). Today at Nir'pa Co, below freezing temperatures and minimal precipitation between November and April limit watershed erosion and the transport of clastic material to the lake during the cold season (Figure 2c). At the same time, cold season ice cover precludes sediment influx to Nir'pa Co while also limiting autochthonous biological productivity. As such, sediment deposition at the lake is largely restricted to the warm summer months when clastic material can be mobilized by monsoonal precipitation after above freezing temperatures remove snow cover from the watershed and ice cover from the lake. Watershed and in-lake productivity also increase during this time, although the degree of productivity is controlled by multiple factors, including average temperature, precipitation, pH, nutrient availability, and turbidity (Carpenter et al., 1985; Catalan et al., 2009).

Given the highly seasonal climate at Nir'pa Co and the regional dominance of the ISM on the summer hydrologic regime, we interpret Nir'pa Co's clastic sediment record as reflecting watershed and depositional processes that are linked to summer climatic conditions associated with the ISM. The lithic fraction,

which averages more than half of the sediment total, is by far the dominant component of Nir'pa Co's sediment archive record. Of this component, silt is the primary grain size fraction, averaging 72.9% followed by %clay and %sand. Modern grain size distributions show that silt and clay are relatively evenly distributed across Nir'pa Co's profundal zone although with an antiphased relationship (Figure 2). Increases in one constituent, therefore, necessarily lead to the reduction in the other. We suggest that the downcore antiphased relationship between %silt and %clay reflects variations in runoff intensity, such that silt (clay) content would increase (decrease) when runoff intensity was enhanced (diminished). This is supported by the similarities between %silt and %lithics ( $r = 0.51$ ,  $p < 0.001$ ), which are interpreted as the relative contribution of clastic material delivered to the lake (Sly, 1978). We suggest %lithics is primarily controlled by summer precipitation, whereby enhanced rainfall results in greater lithic mobilization in the watershed. At the same time, %silt abundances reflect increased runoff energy during times of greater lithic influx.

Downcore variations in %sand are distinct from those in lithics, silt, and clay, but with transitions that were contemporaneous with changes in silt, clay, and lithics (Figure 5). This suggests that different but still climatically related processes resulted in changes in the proportion of sand deposited at the core site. Today, sand abundance is clearly linked to lake levels with minimum sand in profundal sites and increasing abundances toward the littoral and inlet regions. Because much of Nir'pa Co's bathymetry is steep sided with a flat bottom, changes in lake level will not greatly increase the proximity of the littoral zone for most of the lake's basin (Håkanson, 1982). At the lake's shallow north end, however, small changes in lake level will more significantly reduce the distance between the core site and the point at which seasonal fluvial discharge enters the lake. For example, a lake level decrease of ~1.5 m would increase the proximity of fluvial inputs and the core site by approximately 130 m (Figure 2b). Although encroachment of the littoral zone at other points around the lake basin might also be important, the net result of increased sand with lower lake levels would remain consistent. We therefore interpret %sand as a lake level indicator such that increased sandiness reflects lower lake levels with more proximal fluvial discharge and reduced sandiness reflects higher lake levels and more distal fluvial discharge relative to the core site. That sand increased during times when silt and lithics decreased, is consistent with our interpretation because if increased sandiness were related to runoff energy, we would expect it to increase in phase with silt and lithics, not decrease as is observed.

### MS and Si/Ti

The MS and Ti abundances in lacustrine sediments have been widely used as indicators of the contribution of terrestrial clastic material (Metcalfe et al., 2010; Seltzer et al., 2002). At Nir'pa Co, MS and Ti closely track changes in %lithics and silt although with important differences, particularly after 1.3 ka, generally supporting the hypothesis of terrestrial erosion control. Subtle differences between Ti and MS, however, indicate that processes other than terrestrial input may be reflected in the MS profile.

### Late-Holocene ISM rainfall at Nir'pa Co

Based on the sedimentological characteristics of Nir'pa Co's clastic sediment fraction, we identified three distinct multi-century-scale phases of hydroclimate variability during the last 3.3 ka within a larger trend of generally increasing precipitation (Figure 6). Two periods of elevated lithic and silt abundance with low clay and sand content occurred between 3.3 and 2.4 ka and 1.3 ka and the present, suggesting wetter conditions and a

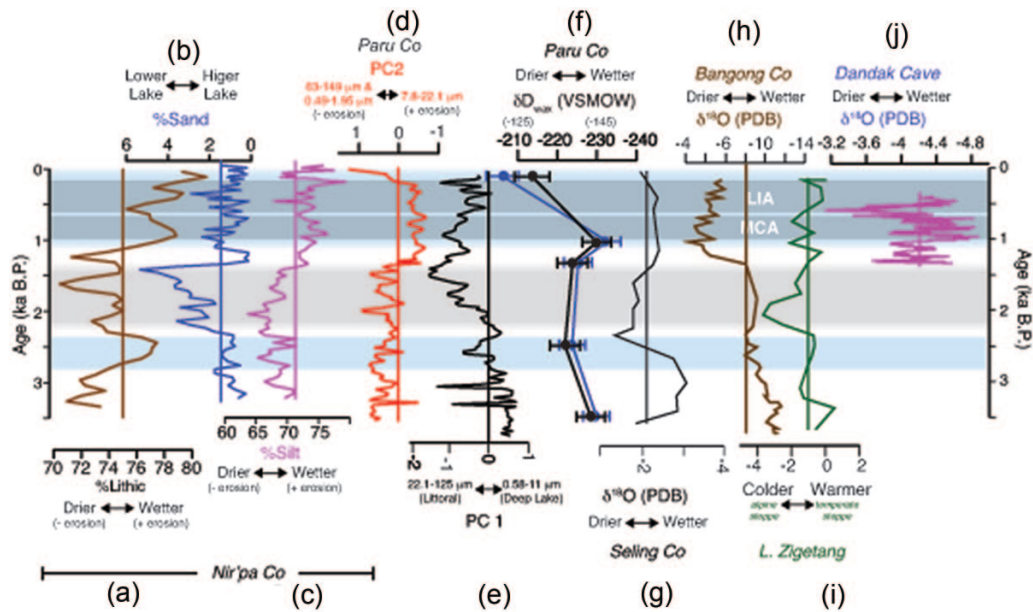


**Figure 6.** Comparison of results from (a–c) Nir'pa Co with regional (d–j) paleoclimate records. Nir'pa Co (a) %lithics, (b) %sand on a reversed axis, and (c) %silt; Paru Co (d) PC1 lake-level curve, (e) PC2 erosion curve, and (f) leaf wax hydrogen isotopes; (g) Seling Co  $\delta^{18}\text{O}$  of calcite; (h) Bangong Co  $\delta^{18}\text{O}$  of calcite; (i) Lake Zigetang pollen biome index of relative surface air temperature; and (j) Dandak Cave  $\delta^{18}\text{O}$  of calcite. Blue horizontal bars indicate pluvial phases, while the gray bar indicates aridity. Vertical lines as in Figures 4 and 5.

strengthened ISM. Although MS does not show a strong increase during the earliest inferred wet period between 3.3 and 2.4 ka, it does increase significantly after 1.3 ka in step with lithics, %silt, and Ti, indicating that the increase in ISM precipitation was large enough to register in all proxies. The intervening period from 2.4 to 1.3 ka, with its lower silt and lithic content, but elevated sand and clay content, suggests drier conditions with lower lake levels.

Superimposed on these millennial-scale ISM variations were higher frequency century-scale ISM variations; however, these are comparatively minor when considered within the context of the lower frequency variations (Figure 6). In particular, it is notable that relatively minor sedimentological responses are apparent at Nir'pa Co during the MCA (950–800 cal. yr BP). Although subtle and not statistically significant (two-sample *t*-test null hypothesis not rejected), decreasing sand and elevated silt and lithics during the MCA may possibly reflect an increase in ISM rainfall that resulted in higher lake levels and greater watershed erosion during this event (Figure 6a–c). Increasing %sand and slightly reduced lithics and %silt during the LIA from 500 to 200 cal. yr BP may suggest a drier LIA at Nir'pa Co. It is important to stress, however, that sedimentological responses during the MCA and LIA were minor compared to the millennial-scale increase in ISM precipitation on which they are superimposed and that additional records with greater temporal resolution and climatic sensitivity are needed to more robustly investigate MCA and LIA hydroclimate expressions in this region.

#### Late-Holocene productivity at Nir'pa Co

Paleo productivity at Nir'pa Co is interpreted from several indicators, including %OM, OM flux, the elemental abundance and isotopic composition of organic carbon and sedimentary nitrogen, and biogenic silica.

The decreasing trend in %OM at Nir'pa Co from 3.3 ka to 360 cal. yr BP is attributed to dilution from increasing clastic sedimentation as indicated by greater lithic composition and mass accumulation rates, particularly after 1.3 ka (Figures 4 and 5). When considered as flux, OM shows an increasing trend during the late-Holocene that is antiphased with decreasing C:N,

implicating enhanced aquatic productivity as the cause of this trend (Figure 5). Biogenic silica also shows an increasing trend when considered as flux, additionally supporting the idea that aquatic productivity increased through the late-Holocene. At the same time,  $\delta^{13}\text{C}_{\text{org}}$  varies by less than 1 ‰, with the exception of one surface sample that was markedly more negative than the late-Holocene average, suggesting that aquatic productivity was the source of sedimentary organic matter and that only its production intensity changed through time.

#### Late-Holocene ISM variability on the Third Pole

Despite generally more arid late-Holocene conditions (Bird et al., 2014; Cai et al., 2012; Gasse et al., 1996; Mügler et al., 2010; Zhu et al., 2008), comparison of Nir'pa Co results with other Third Pole paleoclimate records indicates periods of coherent hydroclimatic variability on the central and eastern Tibetan Plateau (Figure 6). At nearby Paru Co, for example, reconstructed lake levels were higher between 3.3 and 2.5 ka and 1.3 ka and the present, with an intervening period of declining lake level between 2.4 and 1.3 ka (Figure 6d). Erosion at Paru Co was also significantly enhanced after 1.3 ka, consistent with trends at Nir'pa Co (Figure 6e). Although low resolution, the hydrogen isotopic composition of leaf wax *n*-alkanes ( $\delta\text{D}_{\text{wax}}$ ) at Paru Co broadly suggests similar late-Holocene hydrologic variability with lower  $\delta\text{D}_{\text{wax}}$  corresponding to periods of increased precipitation, erosion, and high lake levels and higher  $\delta\text{D}_{\text{wax}}$  corresponding to periods of reduced ISM precipitation, reduced erosion, and lower lake levels at Paru Co and Nir'pa Co (Figure 6f).

At Seling Co, the largest lake in Tibet and located approximately 370 km northwest of Nir'pa Co, late-Holocene  $\delta^{18}\text{O}_{\text{cal}}$  values were relatively low from 3.3 to 2.4 ka and after 1.4 ka, suggesting wetter conditions during these times (Figure 6g; Gu et al., 1993). Between 2.4 and 1.4 ka, higher  $\delta^{18}\text{O}_{\text{cal}}$  at Seling Co suggests enhanced aridity. Similar trends are noted in grain size, mineralogical, and geochemical proxies at Nam Co, the second largest lake on the Tibetan Plateau, which is approximately 180 km northwest of Nir'pa Co (Mügler et al., 2010; Zhu et al., 2008). A generally stable environment is suggested for Nam Co between 4 and 1.6 ka with a marked period of aridity between 1.6 and



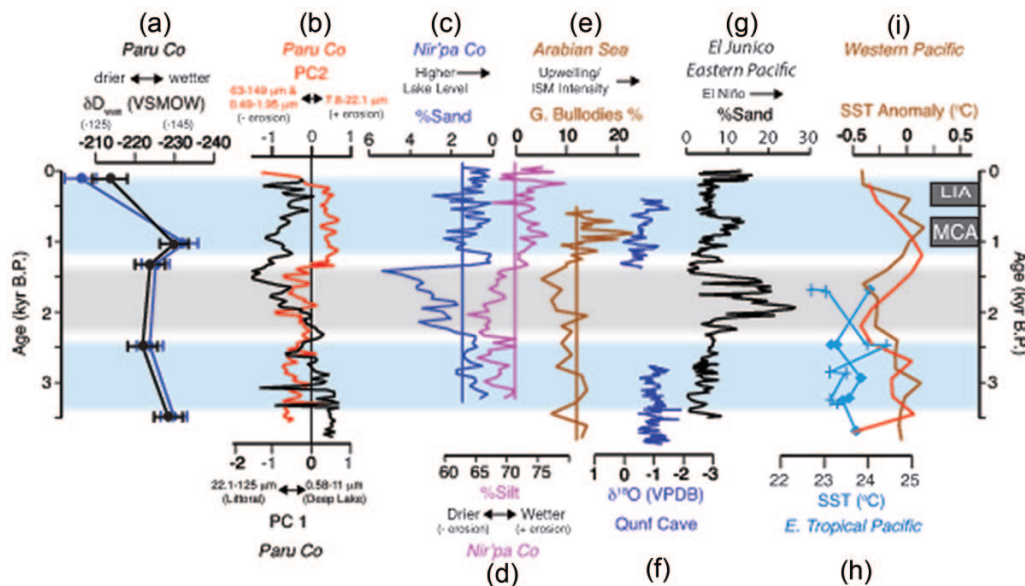


**Figure 7.** Comparison of the (a, b) Paru Co and (c, d) Nir'pa Co results with other more distal ISM records from (e) the Arabian Sea marine sediment cores and (f) Qunf Cave  $\delta^{18}\text{O}$ , Oman. Also shown are the (g) El Junco %sand El Niño record and SST reconstructions from (h) the eastern tropical Pacific and (i) Indo-Pacific. Vertical lines as in Figures 4–6.

1.4 ka. After 1.4 ka, wetter conditions persisted until 800 cal. yr BP, after which point aridity was again inferred. Considered as a whole, the similar trends at Seling Co and Nam, Nir'pa Co and Paru Co, particularly since 1.4 ka, suggest regionally similar multi-centennial to millennial-scale hydroclimate on the south-eastern and central Tibetan Plateau.

The hydroclimatic variations inferred from Tibetan lake sediment records are generally similar with inferred changes in surface air temperatures as reconstructed with a pollen biome index technique applied to results from Lake Zigetang (Figure 6i; Herzschuh et al., 2006). Elevated air temperatures are suggested to have persisted between 3.3 and 2.3 ka and after 1.4 ka with cooler air temperatures between 2.3 and 1.4 ka. This suggests that increased ISM precipitation between 3.3 and 2.4 ka and 1.3 ka and the present was broadly associated with warmth on the Tibetan Plateau, whereas reduced ISM rainfall between 2.4 and 1.3 ka coincided with cooler air temperatures. This pattern was also noted for other high lake stands, and precipitation increases during the middle and early Holocene at Paru Co (Bird et al., 2014).

In contrast with the largely similar expression of ISM variability on central and eastern Tibetan Plateau, the Bangong Lake  $\delta^{18}\text{O}$  record from western Tibet shows different trends during the last 3 ka (Figure 6h; Gasse et al., 1996). Increasing  $\delta^{18}\text{O}$  after 3.3 ka is interrupted at 2.4 ka by a period of steady to lower  $\delta^{18}\text{O}$  that lasted until 1.3 ka. After 1.3 ka,  $\delta^{18}\text{O}$  at Bangong Lake increased abruptly to maximum late-Holocene values that then decreased slowly. It is possible that the Bangong Lake  $\delta^{18}\text{O}$  data reflect regional changes in effective moisture, with the last 1.3 ka being a period of considerably higher evaporation and reduced ISM precipitation that did not penetrate into western Tibet. This idea is consistent with recent work that showed lake levels in western Tibet were more sensitive to long-term reductions in ISM precipitation than those in the east, which are closer to the source of ISM moisture (Hudson and Quade, 2013). It is also possible that moisture from the mid-latitude westerlies, which has elevated  $\delta^{18}\text{O}$  relative to monsoonal precipitation (Tian et al., 2007), increased during this time as the ISM weakened.

#### Regional late-Holocene ISM expressions

The ISM trends discussed above are also expressed in proxy records more distal to the Tibetan Plateau, but still within the

sphere of ISM influence. A foraminifera-based upwelling record from the Arabian Sea, for example, shows enhanced upwelling, suggesting a strengthened ISM during the two pluvial phases identified at Nir'pa Co between 3.3 and 2.4 ka and 1.3 ka and the present with the latter stronger than the former (Figure 7e; Gupta et al., 2005; Overpeck et al., 1996). Between 2.4 and 1.5 ka, upwelling is reduced relative to the preceding and following periods. The Oman speleothem  $\delta^{18}\text{O}$  record, which has been interpreted as reflecting the northerly (wet) or southerly (dry) position of the Intertropical Convergence Zone (ITCZ), shows relatively little  $\delta^{18}\text{O}$  variability, but contains a hiatus between 2.7 and 1.4 ka (Figure 7f). This may suggest that reduced precipitation during this time, possibly reflecting a southerly mean position of the ITCZ, precluded drip water percolation and calcite formation (Fleitmann et al., 2007).

Although temporally limited, trends in a 900-year-long  $\delta^{18}\text{O}$  record from Dandak Cave, India, show some similarities with the Third Pole records (Figure 6j; Sinha et al., 2006). The initiation of calcite precipitation at Dandak Cave at approximately 1.3 ka coincides with the end of the arid interval at Nir'pa Co between 2.4 and 1.3 ka. This may indicate that a shift to increased precipitation at Dandak Cave at this time permitted calcite to form. Generally low  $\delta^{18}\text{O}$  at Dandak Cave between 1020 and 690 cal. yr BP suggests an interval of enhanced ISM precipitation that coincides with the MCA. This is consistent with another speleothem from Sahiya Cave (30° 36'N, 77° 52'E, 1190 m a.s.l.) that shows low  $\delta^{18}\text{O}$  during the MCA between 1050 and 650 cal. yr BP, indicating enhanced ISM precipitation and moisture delivery from the Bay of Bengal (Sinha et al., 2015). This supports the tentative evidence from Nir'pa Co that the MCA may have been a period of slightly greater ISM precipitation on the central/eastern Tibetan Plateau. Increasing  $\delta^{18}\text{O}$  after 650 and 690 cal yr BP in the Dandak and Sahiya Cave records, respectively, although with variability, and the cessation of calcite precipitation at 390 cal. yr BP at Dandak Cave, suggests a shift to increasing aridity during the LIA that coincides with potentially drier conditions at Nir'pa Co. It is important to stress, however, that the MCA and LIA signals in the Nir'pa Co record are not statistically significant, which suggests that these events were not strongly expressed in at least the south-eastern portion of the Tibetan Plateau. Additional records are needed from this and other regions across Tibet in order to better evaluate the expression of these events and whether or not they were indeed climatically significant intervals.

### Mechanisms of late-Holocene ISM precipitation trends

The largely coherent multi-centennial ISM trends noted in lake sediment records from the central and eastern Tibetan Plateau suggest common, large-scale forcing mechanisms. Although some works suggest that the modern ENSO–ISM relationship was only established during the last 2000 years, previous work investigating Holocene ISM on the Third Pole showed that it closely followed Indo-Pacific SST- and ENSO-like ocean–atmosphere variability on centennial and millennial scales through the Holocene (Bird et al., 2014). Comparison of the Nir’pa Co results and other Third Pole records shows that periods of inferred wet conditions between 3.3 and 2.4 ka and from 1.3 ka to the present similarly coincided with Indo-Pacific warming and eastern equatorial Pacific cooling suggestive of La Niña-like conditions (Figure 7h and i; Koutavas et al., 2006; Marchitto et al., 2010). Although SST reconstructions spanning the last 2 ka are not available from the EEP, an El Niño record from El Junco, a crater lake in the Galapagos Islands, provides supporting evidence for late-Holocene ENSO variability that is consistent with SST records from the Indo-Pacific (Figure 7g; Conroy et al., 2008). Generally, low %sand in the El Junco record from 3.3 to 2.4 ka and 1.3 ka to the present is interpreted to reflect reduced precipitation over the lake’s watershed, which occurs today during La Niña conditions. Persistent La Niña-like conditions from 3.3 to 2.4 ka and 1.3 ka to the present is consistent with the Nir’pa Co results and other Third Pole records, which suggest wetter and warmer conditions during these times. Peak %sand at El Junco between 2.4 and 1.3 ka, suggesting persistent El Niño-like conditions, coincides with lake level decreases at Nir’pa Co and Paru Co, aridity at Seling Co and Nam Co, and cooling on the Tibetan Plateau. The suggested occurrence of El Niño-like conditions between 2.4 and 1.3 ka is consistent with Indo-Pacific cooling and the modern relationship between El Niño, reduced ISM precipitation, and cooling as a result of enhanced Tibetan Plateau snow pack (Shaman and Tziperman, 2005). Similar ENSO patterns are observed at Laguna Pallcacocha, Ecuador, with the exception of the period between 2.4 and 1.7 ka, when fewer than five ENSO events per century were observed and the El Junco record suggests enhanced El Niño-like conditions (Moy et al., 2002). The El Junco record, however, may better reflect EEP ENSO-like variability because its location in the Galapagos Islands is more directly linked to Pacific SST and convective activity (Conroy et al., 2008).

The relatively minor expressions of the MCA and LIA in the higher resolution record from Nir’pa Co suggest that lower frequency climate processes, particularly those acting in the Indo-Pacific, may have been more fundamental in determining the mean state of the late-Holocene ISM. Still, that the ISM appears to have strengthened during the MCA and weakened during the LIA is consistent with evidence for La Niña-like and El Niño-like conditions during these events, respectively (Mann et al., 2009).

### Summary and conclusion

The Nir’pa Co sediment record provides a detailed view of late-Holocene ISM variability from the southeastern Tibetan Plateau spanning the last 3.3 ka. Within the context, a generally weakened late-Holocene ISM, two pluvial phases are identified. The strongest pluvial phase, which is recognized in other records from the central and eastern Tibetan Plateau, occurred between 1.3 ka and the present. The second, less intense pluvial phase occurred between 3.3 and 2.4 ka.

Between these pluvial phases, a pronounced arid interval occurred between 2.4 and 1.3 ka. Other paleoclimate records from the Third Pole also indicate aridity during this time, suggesting that this was a widespread event. The two pluvial phases occurred in conjunction with warmer surface air temperatures on the

Tibetan Plateau, elevated SST in the Indo-Pacific, and lower SST in the EEP. These conditions are consistent with a La Niña-like mean state in the tropical Pacific, suggesting that Indo-Pacific ocean–atmosphere variability contributed to these events. This idea is supported by a lake sediment record from El Junco in the ENSO-sensitive Galapagos Islands, which suggests La Niña-like conditions occurred during inferred pluvial phases at Nir’pa Co. Conversely, aridity at Nir’pa Co between 2.4 and 1.3 ka occurred in conjunction with reduced Indo-Pacific SST and cooling on the Tibetan Plateau, which are suggestive of enhanced El Niño-like conditions. The El Junco record again supports this idea, showing the greatest increase in %sand during the late-Holocene, which has been interpreted as reflecting enhanced El Niño conditions. These associations between variations in ISM precipitation, Tibetan Plateau surface air temperatures, and Pacific ocean–atmosphere variability are consistent with modern relationships observed in the instrumental record, whereby El Niño/El Niño-like conditions produce reductions in ISM precipitation and La Niña/La Niña-like conditions enhance the ISM.

Although the above ISM phases are noted in multiple records from the Third Pole, the Bangong Co record from western Tibet shows opposite trends during the late-Holocene. This suggests that ISM variability during the last 3 ka differed across the Tibetan Plateau. This may reflect the inability of the ISM to exert a strong influence across the Tibetan Plateau as a result of its generally weakened mean state during the late-Holocene. As a result, evaporation in western Tibet may have increased with little moderation by the two pluvial events noted in the central and eastern Tibetan Plateau. This is consistent with east–west asymmetry in Holocene lake level trends that show greater evaporation sensitivity in western Tibet. The last 1000 years may also have experienced increased moisture from westerly sources as a result of strengthened westerlies that delivered isotopically lighter precipitation.

Superimposed on the millennial-scale ISM variations noted above were minor higher frequency but lower amplitude changes in ISM precipitation. Although subtle and not statistically significant, possible increases in ISM rainfall and lake levels occurred during the MCA, while reductions in ISM rainfall and lower lake levels are suggested for the LIA. These hydroclimate expressions of the MCA and LIA are consistent with regional evidence from speleothems and recent work combining proxy records and climate model simulations suggesting a La Niña-like mean state in Pacific ocean–atmosphere system during the MCA and an El Niño-like mean state during the LIA. Additional records with improved spatial and temporal resolutions are needed, however, to better assess the apparently subtle expressions of the MCA and LIA in the ISM region.

The patterns and mechanisms of late-Holocene ISM variability identified in the Nir’pa Co and other Third Pole records are consistent with those identified for the early- and middle-Holocene (e.g. Bird et al., 2014). This suggests that the tropical Pacific’s response to warming (Clement et al., 1996; England et al., 2014; Marchitto et al., 2010) may continue to enhance ISM precipitation on the Tibetan Plateau, as has been apparent from the expansion of lakes across the plateau, but particularly in the central and eastern sections over the last few decades (Lei et al., 2013). Additional and higher resolution records are needed from the Third Pole region, however, in order to confirm our findings, evaluate their spatiotemporal coherence, and investigate additional controls on multi-decadal ISM rainfall through the Holocene (e.g. solar and Atlantic ocean–atmosphere variability).

### Acknowledgements

The authors thank the Limnological Research Center at the University of Minnesota and the Large Lakes Observatory at the University of Minnesota, Duluth, for use of their facilities and their expertise. John Southon at the University of California,

Irvine, Keck Carbon Cycle AMS facility is additionally recognized for his help with radiocarbon dating. All original data presented in this paper are publicly available via the NOAA Paleoclimate Database (<https://www.ncdc.noaa.gov/paleo/study/20368>).

## Funding

This research was supported by the United States National Science Foundation (grant nos 1405072 and 1023547) and the National Natural Science Foundation of China (grant no. 41150110153).

## References

- Appleby PG and Oldfield F (1983) The assessment of  $^{210}\text{Pb}$  data from sites with varying sedimentation accumulation rates. *Hydrobiologia* 103: 29–35.
- Ashok K, Guan Z and Yamagata T (2001) Impact of the Indian Ocean Dipole on the relationship between the Indian monsoon rainfall and ENSO. *Geophysical Research Letters* 28: 4499–4502.
- Ashok K, Guan Z, Saji N et al. (2004) Individual and combined influences of ENSO and the Indian Ocean dipole on the Indian summer monsoon. *Journal of Climate* 17: 3141–3155.
- Berkelhammer M, Sinha A, Stott L et al. (2012) An abrupt shift in the Indian monsoon 4000 years ago. In: Giosan L, Fuller DQ, Nicoll K, et al. (eds) *Climates, Landscapes, and Civilizations*. Washington, DC: AGU, pp. 75–87.
- Bird BW, Abbott MB, Vuille M et al. (2011) A 2300-year-long annually resolved record of the South American summer monsoon from the Peruvian Andes. *Proceedings of the National Academy of Sciences* 108: 8583–8588.
- Bird BW, Polisar PJ, Lei Y et al. (2014) A Tibetan lake sediment record of Holocene Indian summer monsoon variability. *Earth and Planetary Science Letters* 399: 92–102.
- Blaauw M and Christen JA (2011) Flexible paleoclimate age-depth models using an autoregressive gamma process. *Bayesian Analysis* 6: 457–474.
- Cai Y, Zhang H, Cheng H et al. (2012) The Holocene Indian monsoon variability over the southern Tibetan Plateau and its teleconnections. *Earth and Planetary Science Letters* 335–336: 135–144.
- Carpenter SR, Kitchell JF and Hodgson JR (1985) Cascading trophic interactions and lake productivity. *BioScience* 35: 634–639.
- Catalan J, Pla S, García J et al. (2009) Climate and  $\text{CO}_2$  saturation in an alpine lake throughout the Holocene. *Limnology and Oceanography* 54: 2542–2552.
- Chen J, Chen F, Feng S et al. (2015) Hydroclimatic changes in China and surroundings during the Medieval Climate Anomaly and Little Ice Age: Spatial patterns and possible mechanisms. *Quaternary Science Reviews* 107: 98–111.
- Choubert G, Faure-Muret A and Chanteux P (1983) *Atlas géologique du monde*. Paris: UNESCO.
- Clement AC, Seager R, Cane MA et al. (1996) An ocean dynamical thermostat. *Journal of Climate* 9: 2190–2196.
- Conroy JL, Overpeck JT, Cole JE et al. (2008) Holocene changes in eastern tropical Pacific climate inferred from a Galápagos lake sediment record. *Quaternary Science Reviews* 27: 1166–1180.
- Dearing J (1997) Sedimentary indicators of lake-level changes in the humid temperate zone: A critical review. *Journal of Paleolimnology* 18: 1–14.
- England MH, McGregor S, Spence P et al. (2014) Recent intensification of wind-driven circulation in the Pacific and the ongoing warming hiatus. *Nature Climate Change* 4: 222–227.
- Fleitmann D, Burns SJ, Mangini A et al. (2007) Holocene ITCZ and Indian monsoon dynamics recorded in stalagmites from Oman and Yemen (Socotra). *Quaternary Science Reviews* 26: 170–188.
- Gadgil S (2003) The Indian monsoon and its variability. *Annual Review of Earth and Planetary Sciences* 31: 429–467.
- Gasse F, Fontes JC, Van Campo E et al. (1996) Holocene environmental changes in Bangong Co basin (Western Tibet) – Part 4: Discussion and conclusions. *Palaeogeography, Palaeoclimatology, Palaeoecology* 120: 79–92.
- Goswami BN, Madhusoodanan MS, Neema CP et al. (2006) A physical mechanism for North Atlantic SST influence on the Indian summer monsoon. *Geophysical Research Letters* 33: L02706.
- Gray AB, Pasternack GB and Watson EB (2010) Hydrogen peroxide treatment effects on the particle size distribution of alluvial and marsh sediments. *The Holocene* 20: 293–301.
- Gu Z, Liu J, Yuan B et al. (1993) The changes in monsoon influence in the Qinghai-Tibetan Plateau during the past 12,000 years. Geochemical evidence from the L. Selin sediments. *Chinese Science Bulletin* 38: 61–64.
- Gupta AK, Das M and Anderson DM (2005) Solar influence on the Indian summer monsoon during the Holocene. *Geophysical Research Letters* 32: L17703.
- Håkanson L (1982) Lake bottom dynamics and morphometry: The dynamic ratio. *Water Resources Research* 18: 1444–1450.
- He Y, Theakstone WH, Zhonglin Z et al. (2004) Asynchronous Holocene climatic change across China. *Quaternary Research* 61: 52–63.
- Heiri O, Lotter AF and Lemcke G (2001) Loss on ignition as a method for estimating organic and carbonate content in sediments: Reproducibility and comparability of results. *Journal of Paleolimnology* 25: 101–110.
- Herzschuh U, Winter K, Wünnemann B et al. (2006) A general cooling trend on the central Tibetan Plateau throughout the Holocene recorded by the Lake Zige tang pollen spectra. *Quaternary International* 154–155: 113–121.
- Hong YT, Hong B, Lin QH et al. (2003) Correlation between Indian Ocean summer monsoon and North Atlantic climate during the Holocene. *Earth and Planetary Science Letters* 211: 371–380.
- Hong YT, Hong B, Lin QH et al. (2005) Inverse phase oscillations between the East Asian and Indian Ocean summer monsoons during the last 12000 years and paleo-El Niño. *Earth and Planetary Science Letters* 231: 337–346.
- Hudson AM and Quade J (2013) Long-term east-west asymmetry in monsoon rainfall on the Tibetan Plateau. *Geology* 41: 351–354.
- Koutavas A, Olive GC and Lynch-Stieglitz J (2006) Mid-Holocene El Niño–Southern Oscillation (ENSO) attenuation revealed by individual foraminifera in eastern tropical Pacific sediments. *Geology* 34: 993–996.
- Krishnamurthy V and Kirtman BP (2009) Relation between Indian monsoon variability and SST. *Journal of Climate* 22: 4437–4458.
- Krishnan R and Sugi M (2003) Pacific decadal oscillation and variability of the Indian summer monsoon rainfall. *Climate Dynamics* 21: 233–242.
- Kumar KK, Rajagopalan B, Hoerling M et al. (2006) Unraveling the mystery of Indian monsoon failure during El Niño. *Science* 314: 115–119.
- Lawrimore JH, Menne MJ, Gleason BE et al. (2011) An overview of the Global Historical Climatology Network monthly mean temperature data set, version 3. *Journal of Geophysical Research* 116: D19121.
- Lei Y, Yao T, Bird BW et al. (2013) Coherent lake growth on the central Tibetan Plateau since the 1970s: Characterization and attribution. *Journal of Hydrology* 483: 61–67.
- Liu X, Dong H, Yang X et al. (2009) Late-Holocene forcing of the Asian winter and summer monsoon as evidenced by proxy

- records from the northern Qinghai–Tibetan Plateau. *Earth and Planetary Science Letters* 280: 276–284.
- Mann ME, Zhang Z, Rutherford S et al. (2009) Global signatures and dynamical origins of the Little Ice Age and Medieval Climate Anomaly. *Science* 326: 1256–1260.
- Marchitto TM, Muscheler R, Ortiz JD et al. (2010) Dynamical response of the tropical Pacific Ocean to solar forcing during the early Holocene. *Science* 330: 1378–1381.
- Metcalfe SE, Jones MD, Davies SJ et al. (2010) Climate variability over the last two millennia in the North American Monsoon region, recorded in laminated lake sediments from Laguna de Juanacatlán, Mexico. *The Holocene* 20: 1195–1206.
- Mischke S and Zhang C (2010) Holocene cold events on the Tibetan Plateau. *Global and Planetary Change* 72: 155–163.
- Morrill C, Overpeck JT and Cole JE (2003) A synthesis of abrupt changes in the Asian summer monsoon since the last deglaciation. *The Holocene* 13: 465–476.
- Morrill C, Overpeck JT, Cole JE et al. (2006) Holocene variations in the Asian monsoon inferred from the geochemistry of lake sediments in central Tibet. *Quaternary Research* 65: 232–243.
- Mortlock RA and Froelich PN (1989) A simple method for the rapid determination of biogenic opal in pelagic marine sediments. *Deep Sea Research Part A: Oceanographic Research Papers* 36: 1415–1426.
- Moy CM, Seltzer GO, Rodbell DT et al. (2002) Variability of El Niño/Southern Oscillation at millennial timescales during the Holocene epoch. *Nature* 420: 162–165.
- Mügler I, Gleixner G, Günther F et al. (2010) A multi-proxy approach to reconstruct hydrological changes and Holocene climate development of Nam Co, Central Tibet. *Journal of Paleolimnology* 43: 625–648.
- Overpeck J, Anderson D, Trumbore S et al. (1996) The southwest Indian Monsoon over the last 18000 years. *Climate Dynamics* 12: 213–225.
- Peings Y and Douville H (2010) Influence of the Eurasian snow cover on the Indian summer monsoon variability in observed climatologies and CMIP3 simulations. *Climate Dynamics* 34: 643–660.
- Peterson TC and Vose RS (1997) An overview of the Global Historical Climatology Network temperature database. *Bulletin of the American Meteorological Society* 78: 2837–2849.
- Qiu J (2008) The Third Pole. *Nature* 454: 393–396.
- Schelske CL, Peplow A, Brenner M et al. (1994) Low-background gamma counting: Applications for <sup>210</sup>Pb dating of sediments. *Journal of Paleolimnology* 10: 115–128.
- Seltzer GO, Rodbell DT, Baker PA et al. (2002) Early warming of tropical South America at the last glacial-interglacial transition. *Science* 296: 1685–1686.
- Shaman J and Tziperman E (2005) The effect of ENSO on Tibetan Plateau snow depth: A stationary wave teleconnection mechanism and implications for the South Asian monsoons. *Journal of Climate* 18: 2067–2079.
- Shuman B, Henderson AK, Colman SM et al. (2009) Holocene lake-level trends in the Rocky Mountains, USA. *Quaternary Science Reviews* 28: 1861–1879.
- Sinha A, Cannariato KG, Stott LD et al. (2006) A 900-year (600 to 1500 A.D.) record of the Indian summer monsoon precipitation from the core of the monsoon zone of India. *Geophysical Research Letters* 34: L16707.
- Sinha A, Kathayat G, Cheng H et al. (2015) Trends and oscillations in the Indian summer monsoon rainfall over the last two millennia. *Nature Communications* 6: 6309.
- Sly P (1978) Sedimentary processes in lakes. In: Lerman A (ed.) *Lakes*. New York: Springer, pp. 65–89.
- Stott L, Cannariato K, Thunnell R et al. (2004) Decline of surface temperature and salinity in the western tropical Pacific Ocean in the Holocene epoch. *Nature* 431: 56–59.
- Stuiver M and Reimer PJ (1993) Extended <sup>14</sup>C database and revised CALIB radiocarbon calibration program. *Radiocarbon* 35: 215–230.
- Thompson LG, Yao T, Mosley-Thompson E et al. (2000) A high-resolution millennial record of the South Asian monsoon from Himalayan ice cores. *Science* 289: 1916–1919.
- Tian L, Masson-Delmotte V, Stievenard M et al. (2001) Tibetan Plateau summer monsoon northward extent revealed by measurements of water stable isotopes. *Journal of Geophysical Research* 106: 28081–28088.
- Tian L, Yao T, MacClune K et al. (2007) Stable isotopic variations in west China: A consideration of moisture sources. *Journal of Geophysical Research* 112: D10112.
- Yanhong W, Lücke A, Zhangdong J et al. (2006) Holocene climate development on the central Tibetan Plateau: A sedimentary record from Cuoe Lake. *Palaeogeography, Palaeoclimatology, Palaeoecology* 234: 328–340.
- Zhang P, Cheng H, Edwards RL et al. (2008) A test of climate, sun and culture relationships from an 1810-year Chinese cave record. *Science* 322: 940–942.
- Zhu L, Wu Y, Wang J et al. (2008) Environmental changes since 8.4 ka reflected in the lacustrine core sediments from Nam Co, central Tibetan Plateau. *The Holocene* 18: 831–839.